CrossMark

REGULAR PAPER

Abhishek Kundu · Sudipta De · Murugan Thangadurai · C. L. Dora · Debopam Das

Numerical visualization of shock tube-generated vortex–wall interaction using a fifth-order upwind scheme

Abstract Compressible Navier–Stokes equations are solved using a fifth-order upwind scheme in the AUSM$^+$ framework to visualize a compressible vortex ring generated from a shock tube. The ring impinges on a wall kept near the open end of the tube. The vortex ring has an embedded shock, counter rotating vortex rings ahead of it and a number of small-scale shear layer vortices trailing behind. When this complex configuration impinges on a wall, wall vorticity is lifted and begins to interact with the complex system of vortices. The paper focusses on the features of the resulting flow field by visualizing them on increasingly finer grids. It is shown that though the different grids capture a fairly matching description of the initial turbulent vortex system that propagates towards the wall, small differences existing between them magnify with time. During vortex–wall interaction, some key experimentally observed features are identified on all the grids, but the details of the vortical structure look significantly different on different grids.

Keywords Shock tube-generated vortex · Counter rotating vortex ring · AUSM$^+$ algorithm · Fifth-order upwind scheme · Navier–Stokes equations · Vortex–wall interaction

1 Introduction

When a high-pressure gas separated from the ambient medium by a diaphragm is allowed to flow out of the open end of a shock tube by bursting the diaphragm, a vortex is generated at the open end. The present study concerns the interaction of this vortex with a nearby wall. A number of experiments have been performed to understand the compressible vortex–wall interaction phenomenon. Kontis et al. (2008) reports vortex

A. Kundu
AcSIR-CMERI, CSIR-Central Mechanical Engineering Research Institute, Durgapur, West Bengal 713209, India
E-mail: abhishekkundu45@gmail.com

S. De (✉) · M. Thangadurai
CSIR-Central Mechanical Engineering Research Institute, Durgapur, West Bengal 713209, India
E-mail: sudiptade72@gmail.com
Tel.: +91-343-6452093

M. Thangadurai
E-mail: murugan.thangadurai@gmail.com

C. L. Dora · D. Das
Department of Aerospace Engineering, Indian Institute of Technology Kanpur, Kanpur 208016, India
E-mail: lakshmanadora@gmail.com

D. Das
E-mail: das@iitk.ac.in

formation at driver gas pressure of 3.95, 7.89 and 11.84 bar, the driven section being held at atmospheric pressure. Experiments are conducted using both solid and perforated plates kept at a distance of 100 mm from the shock tube exit. After propagating downstream for a distance, the primary vortex ring develops an embedded shock, and counter rotating vortex rings appear at its downstream end-phenomena which are common to vortices generated at the open end of a shock tube. Secondary vortices of opposite sign are also generated when the primary vortex ring impinges upon the plate. These are seen to be lifted from the wall and pulled towards the primary ring centre. The high-speed schlieren photography of vortex–wall interaction shows the primary vortex near the wall, with another cluster of vortices at a slightly lower radius. One cannot discern the individual wall vortices embedded within the primary, nor can one clearly view the trailing Kelvin–Helmholtz (KH) vortices interacting with the wall. In another experimental study, Murugan and Das (2012) view a similar flow field using high-speed smoke flow visualization. Visualization of the vortical structures improves, but the smaller scale vortices still cannot be isolated. The particle image velocimetry (PIV) images of the flow field in Mariani et al. (2013) show distinct secondary vortices attached to the wall. It should be noted that the PIV technique also cannot capture strong vortex cores (Zare-Behtash et al. 2010) properly, as the PIV particles are pushed to the outer radii by the centripetal force. A numerical method can be used in identifying these structures. Accuracy of a numerical simulation is dependent on the numerical dissipation and dispersion properties of the discretization scheme. A carefully written Navier–Stokes solver can be a very good tool to visualize the regions of strong vortex cores as are present in the current problem. An Euler solver can also be equally good in certain cases, but for vortex–wall interaction the presence of the no-slip wall necessitates the use of a Navier–Stokes solver. In an earlier study (Minota et al. 1997), compressible Navier–Stokes equations were solved to predict the flow field due to impingement of a compressible vortex ring on a solid wall. The wall vortices were identified by the vorticity contours, but the low grid resolution (210×165 points) coupled with a second-order accurate scheme was not sufficient to resolve the finer features of the flow. The low-dissipation fifth-order upwind scheme used in the present paper is necessary to accurately track evolving small-scale vortices triggered by KH-instability, which interact with each other leading to turbulence. The recent paper by San and Kara (2015) is an excellent resource on computation of turbulence generated by KH-instability using various high-order schemes. Besides, such schemes are also useful in computational aeroacoustics and in supersonic combustion, where high temperature and species gradients are present in addition to shock waves (Fiorina and Lele 2007).

In a recent article, Murugan et al. (2016) have numerically studied the dynamics of shock-free and shock-embedded vortices (incident shock Mach number 1.36 and 1.57, respectively) in collision with a wall. Use of a fifth-order upwind scheme together with a low-dissipative and dispersive Runge–Kutta scheme for time integration made it possible to visualize the various states of the primary and the secondary vortices in great details. The maximum grid size used had 2.2 million cells. Some differences were noticed at the early stage between the two grids used (the other was a coarser one with 0.55 million cells). It was commented that 'these differences at the early stage show up later during wall impingement of the vortices'. It is true that key phenomena that have been described in Murugan et al. (2016) based on the coarser grid results are similar on the finer grid, but it still remains to be seen how the details differ at later stages. When a wall is not interacting with the shock tube-generated primary vortex, good match between experiment and numerical computation has already been obtained (Murugan et al. 2011, 2013). Increasing the grid size has resulted mainly in difference in the number, size and positioning of the small-scale shear layer vortices. The situation is not the same when the primary vortex ring drifts towards a nearby wall and interacts with it. The small changes noticed between different grids (or schemes with differing spectral resolution properties) in the early stage of evolution of the vortex may lead to more significant differences later. In this paper, we work with the same scheme as in Murugan et al. (2016), but report results on four different grids for a single pressure ratio between the driver and driven sections of the shock tube. The coarsest has a cell count of 0.55 million [the same as in Murugan et al. (2016)]. The next grids are obtained by doubling the cell count in each co-ordinate direction. Through vorticity contour plots, we show the differences between the results at four different time instants. Our aim is to show how small early differences show up at later stages of evolution of the vortex. Advances have been made in experimental techniques, and observation of small-scale vortical structures in high-speed flow are being reported nowadays (Chen et al. 2013). When these more advanced experimental methods are applied to the present class of problems, the results reported here will allow us to estimate the usefulness of 'implicit large eddy simulation' (ILES) in detecting small-scale features of high-speed vortical flow.

2 Problem definition and numerical method

The computational domain for the interaction of a shock tube-generated vortex with a solid wall is shown in Fig. 1. The driver and driven sections of the shock tube are 165 and 1200 mm long, respectively. The wall is located 300 mm downstream of the open end of the tube, as in Murugan et al. (2016). The inner diameter of the shock tube is 64 mm. In all the figures presented, length is nondimensionalized by this inner diameter. At the open end of the shock tube, we set $x = 0$. The tube thickness is 2.6112 mm. This is the same setup as described in Sect. 2.3 of Murugan et al. (2013). Initially, the driven section and the domain outside the tube is kept at atmospheric conditions with a pressure of 1.01325 bar and temperature of 300 K. Air as ideal gas is the working fluid in the whole domain. The initial pressure in the driver section is 7 times the atmospheric pressure. No-slip conditions are applied at the walls of the tube and the right boundary. Top and left boundaries are treated by the NSCBC boundary condition of Poinsot and Lele (1992). Symmetry boundary condition is applied at the centreline (bottom horizontal line), as we solve the axisymmetric form of the compressible Navier–Stokes equations, given in Murugan et al. (2013).

Four different grids are employed, the details of which are in Table 1.

The AUSM$^+$ scheme (Liou 1996) for solving the compressible Navier–Stokes equations has been used with a six-stage low-dissipation and dispersion Runge–Kutta time stepping scheme for time integration (Calvo et al. 2004). The equations are nondimensionalized using the inner diameter of the shock tube as reference length and a reference Mach number (taken as 1.5) times the ambient speed of sound as the reference velocity. Density and temperature references are taken as the respective ambient conditions. A fifth-order accurate cell-face interpolation formula (Kim and Kim 2005; Halder et al. 2013) calculates the primitive variables at the cell faces:

$$u_{j+\frac{1}{2},L} = \frac{(2u_{j-2} - 13u_{j-1} + 47u_j + 27u_{j+1} - 3u_{j+2})}{60} \tag{1}$$

where $u_{j+\frac{1}{2}}$ stands for the value of any primitive variable at the cell face.

When a shock wave is present, a TVD limiter (Kim and Kim 2005) reduces the stencil size to a more dissipative lower order accurate formula. The AUSM$^+$ implementation has been validated with experimental results for shock tube-generated vortices in Murugan et al. 2011, 2013). In Figs. 2 and 3, we present the smoke flow visualization of a shock tube-generated vortex for the same geometry as mentioned above with driver to driven section pressure ratio of 10:1. For the experiment, there was no nearby wall as in the cases reported here, and the same condition is also maintained in the numerical simulation results shown in the upper half for comparison. In Fig. 2, three rising CRVRs are clearly visible in experiment and simulation. Figure 3 shows a similar comparison at a later time. Note that the overall shape of the vortex is matching and outermost small-scale vortex is also in similar location in both the images, though the dipolar
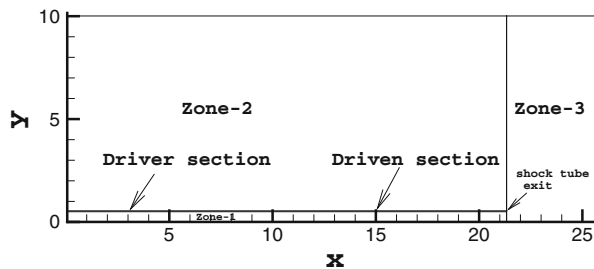

Fig. 1 The computational domain. The right domain boundary is a no-slip wall. It is 300 mm away from the open end of the tube

Table 1 Details of the four grids. $N_x' \times N_y'$ denotes the cells covering the shock tube thickness

Grid	$N_x \times N_y$	Size (million)	Tube grid ($N_x' \times N_y'$)	Final cell count (million)	CPU time ($\frac{t_i}{t_1}$)
G_1	910×610	0.5551	210×10	0.5530	1
G_2	1820×1220	2.2204	420×20	2.2120	3.83
G_3	3640×2440	8.8816	840×40	8.8480	14.86
G_4	7280×4880	35.5264	1680×80	35.3920	58.31

The last column indicates the CPU time on the finer grids relative to the coarsest for a single time step
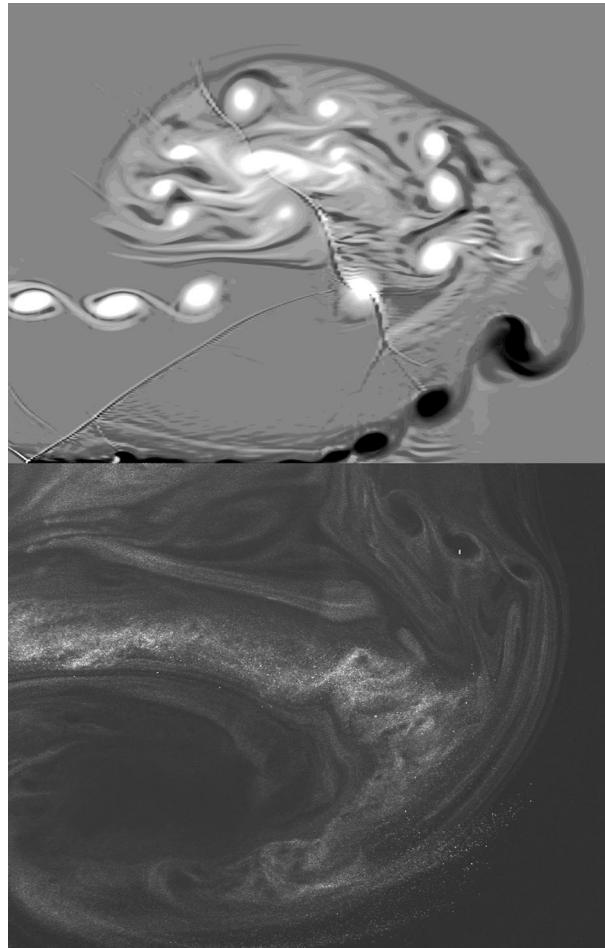
Fig. 2 Numerical vorticity contours (upper half, grid: G_2) and smoke flow visualization for a pressure ratio of 10:1, with no nearby wall at $t = 737$ μs. Time is measured after the shock reaches the shock tube exit

structure is not as clear in the experiment as in simulation. The high-resolution method used here 'appears to achieve many of the properties of subgrid models' (Drikakis 2003) and, therefore, may be termed implicit large eddy simulation (ILES) (Thornber et al. 2007). Assessment of such high-resolution schemes in computing unsteady compressible turbulent flows may be found in Hahn and Drikakis (2005) and Halder et al. (2013).

3 Results and discussion

Shock tube-generated compressible vortices have been characterized by several authors [see, for example, Arakeri et al. (2004); Zare-Behtash et al. 2009); Murugan et al. 2013)]. Brouillette and Hébert (1997) showed that when the incident shock Mach number (M_s) varies between 1.43 and 1.6, an embedded shock appears within the main vortex. In the present case, the incident shock Mach number is 1.51, and accordingly we observe an embedded shock within the primary core. This is shown in Figs. 2 and 3 at $t = 680$ μs ($t = 0$ corresponds to the time when the incident shock is at tube exit). The same figures present an interesting phenomenon—we notice lifting of counter rotating vortex ring (CRVR, marked in the upper frame of Fig. 3) ahead of the primary ring. According to the classification of Brouillette and Hébert (1997), CRVR forms above $M_s = 1.6$. But the high-resolution scheme used here shows the CRVR on all the grids used. On G_1 and G_2, a couple of CRVRs are visible, whereas on the finer grids (G_3 and G_4) they are more in number and smaller in size. By $t = 1480$ μs, one or two such vortices are visible around the periphery of the primary vortex on the coarser grids. The finer grids show several of such small vortices around the periphery
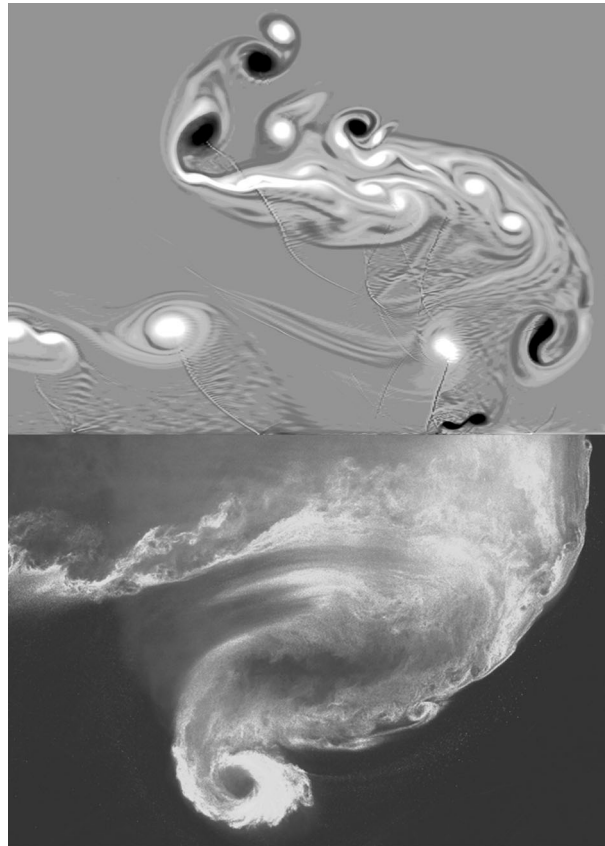
Fig. 3 Numerical vorticity contours (upper half, grid: G_2) and smoke flow visualization for a pressure ratio of 10:1, with no nearby wall at $t = 1587$ μs

of the primary vortex. It is possible that formation of CRVR actually begins earlier than $M_s = 1.6$ [as given in Brouillette and Hébert (1997)], but due to the tiny size of the vortices they have not been detected in experiments so far. At $t = 1480$ μs, G_3 and G_4 show (Fig. 4) one very prominent CRVR ahead of the primary vortex. This CRVR appears to be in the process of forming a dipole by pairing up with a shear layer vortex. This CRVR is not present on the coarser grids (Fig. 5). Also the number, size and position of the shear layer vortices with respect to the primary core vary visibly between grids at this time. Such early differences are likely to have an impact on the flow development later when the primary ring expands radially along the surface of the solid wall. This is shown in Figs. 6 and 7 at $t = 1880$ μs. At this time the vortex has already impinged on the wall and is propagating radially outwards (here, upwards). The presence of the CRVRs on the two finer grid cases has changed the shape of the primary vortex compared to its shape on the coarser grids, which looks more stretched in the radial direction. This figure also shows that even at such early moments of vortex–wall interaction, it is impossible to have a very close match between the results of different grids in the fine-scale details. All of them show vortex stretching, lifting of wall vorticity and presence of shocklets, but the smaller scale shear layer vortices (which the primary vortex collects during its journey toward the flat plate) and opposite signed CRVR and wall vortices do not have much agreement in their shape, size and location. Figures 8 and 9 merely reassert this fact. Here, at $t = 2480$ μs, the shape of the vortex is similar on G_2 and G_3, G_1 shows a shooting dipole at the edge, and G_4 displays a more compact shape of the primary vortex. All of them, however, agree on the fact that there are two distinct clusters of concentrated vortices. The first one is the primary vortex with its associated shear layer vortices and also secondary wall and CRVR vorticity. The second cluster is immediately behind where impinging shear layer vortices interact with lifted wall vorticity and shed secondary vorticity from the expanding primary vortex. The corresponding numerical schlieren images are presented in Figs. 10, 11, 12 and 13, which show the embedded shock waves very well. For a similar vortex–wall interaction problem, Kontis
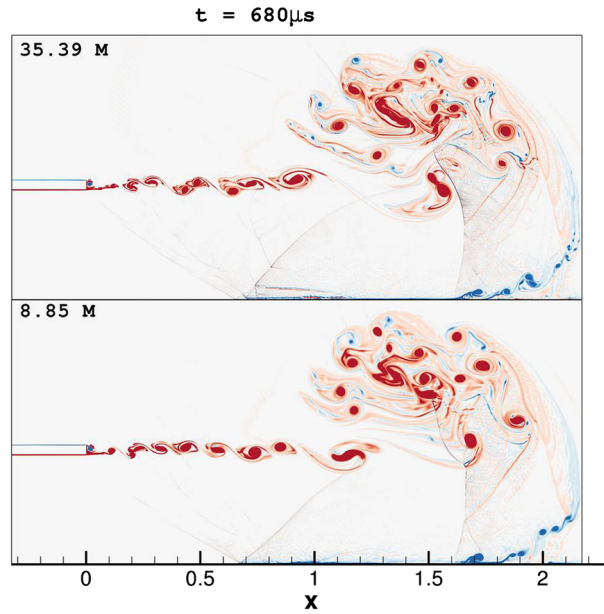
Fig. 4 Vorticity contours at $t = 680$ μs on G_3 (*lower frame*) and G_4. Plotted contour levels: -10 to 10 at an interval of 1, excluding 0; also ± 0.5, ± 0.25, ± 0.15. Vorticity values are nondimensionalized by the reference length and velocity. The location of the *x*-axis has been reset in the figure so that vortex location from the shock tube exit is clearly indicated
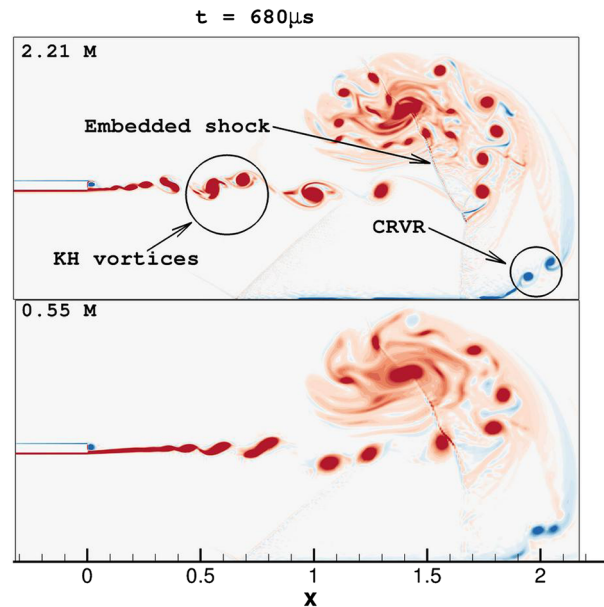

Fig. 5 Vorticity contours at $t = 680$ μs on G_1 (lower frame) and G_2. Same contour levels have been plotted as in Fig. 2

et al. (2008) commented that 'a number of shocklets is produced emanating from the vortex core'. Figures 12 and 13 show these shocklets.

The CRVR formation that has been reported here for M_s has not been experimentally observed so far, to the best of our knowledge. On rolling up of small vortices along a vortex sheet, Sun and Takayama (2003) commented: 'numerical mechanism of the rolling up in numerical simulation is still a controversial issue'. This remark was based on the observation that on fine grids numerical results were 'polluted' by small-scale vortices which were not seen in experimental photos. They considered the possibility of the integrated
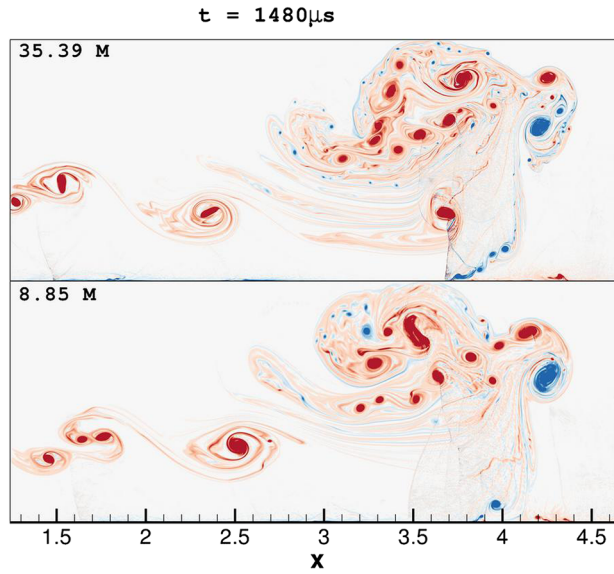
Fig. 6 Vorticity contours at $t = 1480$ μs on G_3 (*lower frame*) and G_4. Same contour levels have been plotted as in Fig. 2
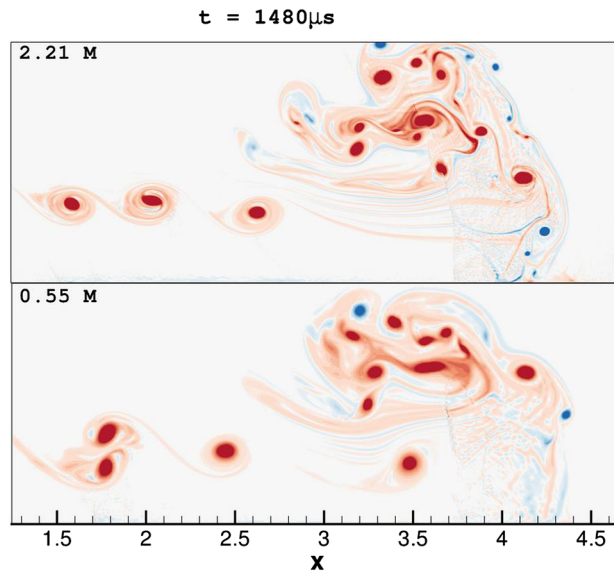

Fig. 7 Vorticity contours at $t = 1480$ μs on G_1 (*lower frame*) and G_2. Same contour levels have been plotted as in Fig. 2

density information across the test section missing the small-scale vortices due to three-dimensional perturbations in the vortices. But then there were cases where the small vortices in simulation became so large that standard optical experimental method would certainly be able to detect them, but they did not. On the other hand, there have been recent reports on improved experimental techniques resolving slipstream-generated instability vortices (Tao et al. 2015). Until such newer experimental methods are applied to the present problem, we need to exercise caution in interpreting the numerical results presented here.

4 Concluding remarks

High-resolution Navier–Stokes simulation results are presented for shock tube-generated compressible vortex–wall interaction. At an incident shock Mach number of 1.51, we notice formation of counter rotating
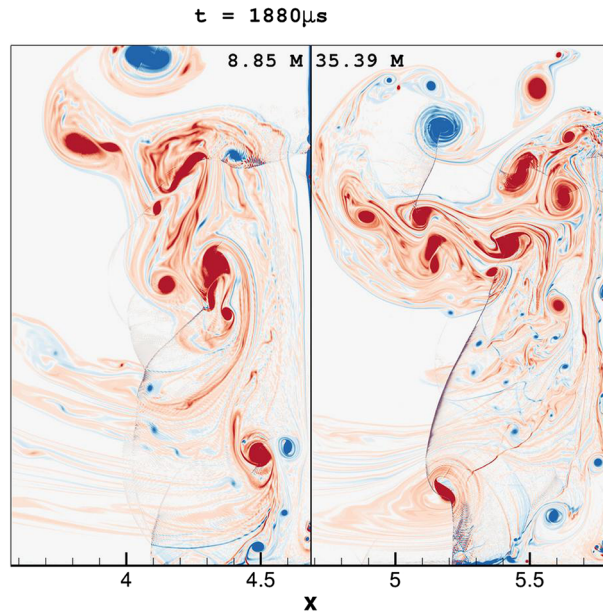
t = 1880µs

Fig. 8 Vorticity contours at $t = 1880$ µs on G_3 (*left frame*) and G_4. The right edge of each frame is the location of the wall. Same contour levels have been plotted as in Fig. 2
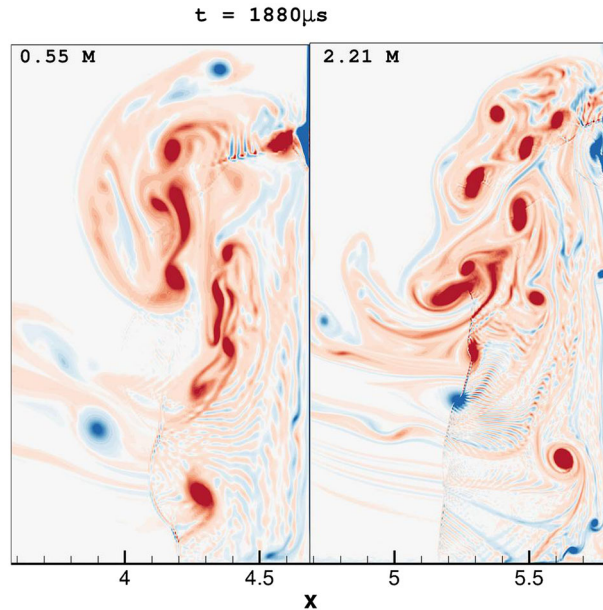
t = 1880µs

Fig. 9 Vorticity contours at $t = 1880$ µs on G_1 (*left frame*) and G_2. The right edge of each frame is the location of the wall. Same contour levels have been plotted as in Fig. 2

vortex rings—a phenomenon that was reported to occur starting from a Mach number of 1.6. Comparison of results on four different grids indicates that shear layer roll-up behind the shock tube-generated vortex starts closer to the shock tube on finer grids. These small-scale vortices interact with the embedded shock and penetrate into the primary core to give it an elliptic shape. The shape, number and position of the shear layer
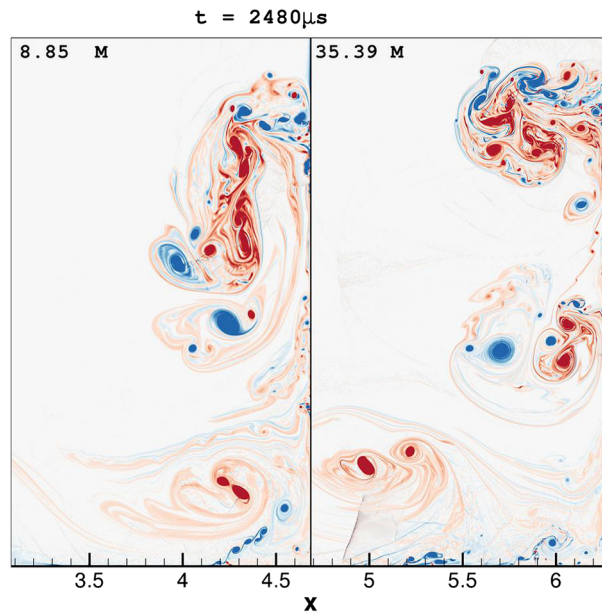
Fig. 10 Vorticity contours at $t = 2480 \mu s$ on G_3 (*left frame*) and G_4. The wall is at the right vertical edge. Same contour levels have been plotted as in Fig. 2
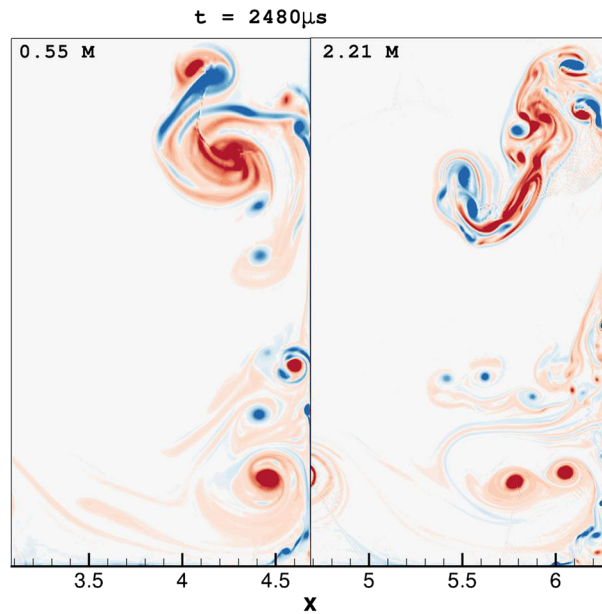

Fig. 11 Vorticity contours at $t = 2480 \mu s$ on G_1 (*left frame*) and G_2. The wall is at the right vertical edge. Same contour levels have been plotted as in Fig. 2

vortices vary within the primary core on different grids. These early differences lead to more significant differences in the vortex structure when it impinges on the solid wall at a later time, though key phenomena such as wall vortex lift-off, stretching of the primary vortex and shocklet formation from its core are all visible on the four grids. Some authors have relied on use of turbulence models for realistic computation of
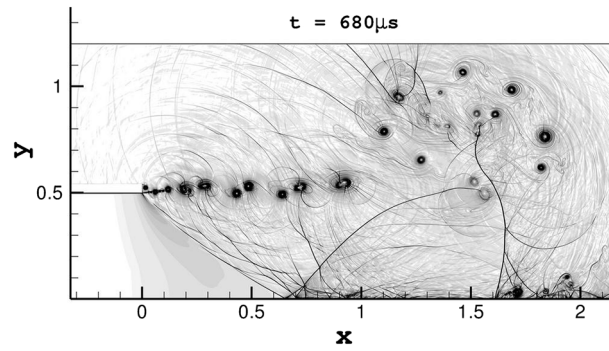
Fig. 12 Numerical schlieren on G_4 at $t = 1480$ µs. 20 contour levels have been plotted between 1 and 20. In addition, 0.4, 0.5 and 1.5 levels are also plotted

Fig. 13 Numerical schlieren on G_4 at $t = 1480$ µs. 20 contour levels have been plotted between 1 and 20. In addition, 0.4, 0.5 and 1.5 levels are also plotted
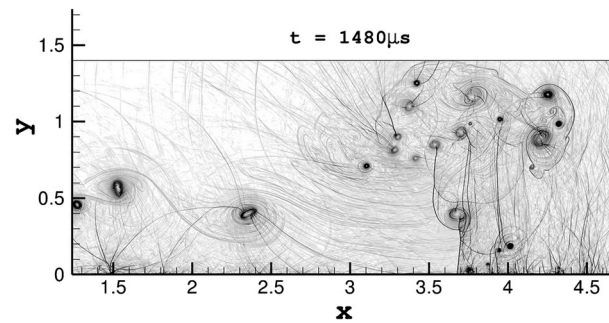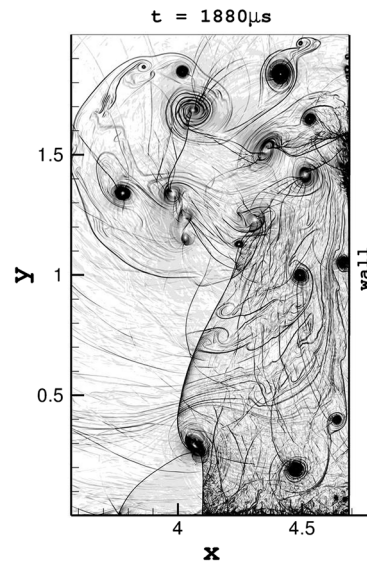

Fig. 14 Numerical schlieren on G_4 at $t = 1880$ µs. 10 contour levels have been plotted between 1 and 10. The wall is at the right vertical edge
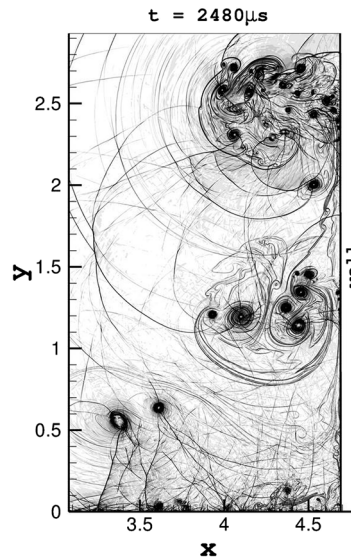
Fig. 15 Numerical schlieren on G_4 at $t = 2480$ μs. 10 contour levels have been plotted between 1 and 10. The wall is at the right vertical edge

similar flow fields. The model-free approach that has been pursued here needs further assessment, particularly vis-à-vis more modern experimental techniques that are capable of visualizing small-scale vortex roll-up from shear layers.

References

Arakeri JH, Das D, Krothapalli A, Lourenco L (2004) Vortex ring formation at the open end of a shock tube: a particle image velocimetry study. Phys Fluids 16(4):1008–1019

Brouillette M, Hébert C (1997) Propagation and interaction of shock-generated vortices. Fluid Dyn Res 21:159–169

Calvo M, Franco JM, Rández L (2004) A new minimum storage Runge–kutta scheme for computational acoustics. J Comput Phys 201:1–12

Chen Z, Yi SH, Tian LF, He L, Zhu YZ (2013) Flow visualization of supersonic laminar flow over a backward-facing step via NPLS. Shock Waves 23:299–306

Drikakis D (2003) Advances in turbulent flow computations using high-resolution methods. Prog Aerosp Sci 39:405–424

Fiorina B, Lele SK (2007) An artificial nonlinear diffusivity method for supersonic reacting flows with shocks. J Comput Phys 222:246–264

Hahn M, Drikakis D (2005) Large eddy simulation of compressible turbulence using high-resolution methods. Int J Numer Meth Fluids 47:971–977

Halder P, De S, Sinhamahapatra KP, Singh N (2013) Numerical simulation of shock-vortex interaction in Schardin's problem. Shock Waves 23:495–504

Kim KH, Kim C (2005) Accurate, efficient and monotonic methods for multi-dimensional compressible flows part II: multi-dimensional limiting process. J Comput Phys 208:570–615

Kontis K, An R, Zare-Behtash H, Kounadis D (2008) Head-on collision of shock wave induced vortices with solid and perforated walls. Phys Fluids 20(016104):1–17

Liou MS (1996) A sequel to AUSM: AUSM$^+$. J Comput Phys 129:364–382

Mariani R, Kontis K, Gongora-Orozco N (2013) Head on collisions of compressible vortex rings on a smooth solid surface. Shock Waves 23:381–398

Minota T, Nishida M, Lee MG (1997) Shock formation by compressible vortex ring impinging on a wall. Fluid Dyn Res 21:1–17

Murugan T, Das D (2012) Experimental study on a compressible vortex ring in collision with a wall. J Vis 15:321–332

Murugan T, De S, Dora CL, Das D (2011) Numerical simulation and PIV study of compressible vortex ring evolution. Shock Waves 22:69–83

Murugan T, De S, Dora CL, Das D, Kumar PP (2013) A study of the counter-rotating vortex rings interacting with the primary vortex ring in shock tube generated flows. Fluid Dyn Res 45:1–20

Murugan T, De S, Sreevatsa A, Dutta S (2016) Numerical simulation of a compressible vortex-wall interaction. Shock Waves. doi:10.1007i/s00193-015-0611-2

Poinsot TJ, Lele SK (1992) Boundary conditions for direct simulations of compressible viscous flows. J Comput Phys 101:104–129

San O, Kara K (2015) Evaluation of riemann flux solvers for weno reconstruction schemes: Kelvin–helmholtz instability. Comput Fluids 117:24–41

Sun M, Takayama K (2003) A note on numerical simulation of vortical structures in shock diffraction. Shock Waves 13:25–32

Tao Y, Fan X, Zhao Y (2015) Flow visualization for the evolution of the slipstream in steady shock reflection. J Vis 18:21–24

Thornber B, Mosedale A, Drikakis D (2007) On the implicit large eddy simulations of homogeneous decaying turbulence. J Comput Phys 226:1902–1929

Zare-Behtash H, Gongora-Orozco N, Kontis K (2009) Global visualization and quantification of compressible vortex loops. J Vis 12(3):233–240

Zare-Behtash H, Kontis K, Gongora-Orozco N, Takayama K (2010) Shock-wave induced vortex loops emanating from nozzles with singular corners. Shock Waves 49:1005–1019